Aerospace Systems (2023) 6:37–51
https://doi.org/10.1007/s42401-022-00185-3

ORIGINAL PAPER

Hybrid feedback pseudospectral method for geostationary debris removal using solar radiation pressure and impulsive thrusts

Hao Mei[1] · Christopher J. Damaren[1] · Xingqun Zhan[2]

Received: 2 August 2022 / Revised: 18 September 2022 / Accepted: 2 December 2022 / Published online: 21 December 2022

Abstract

This paper proposes a hybrid feedback pseudospectral (PS) method for solving hybrid non-convex non-linear optimal control problems. The hybrid dynamic system is defined as a continuous dynamic system with discontinuities in state, and the discontinuities are governed by discrete dynamic equations. First, the local Legendre–Gauss–Lobatto (LGL) PS method is extended to a hybrid LGL PS method which is capable of solving hybrid non-linear optimal control problems. The extension is accomplished by breaking the state continuity constraints between the segments and governing the dynamics of the LGL points on segment boundaries using discrete dynamic equations. Then, a hybrid feedback PS method is proposed, in which a hybrid linear feedback controller is developed to stabilize the open-loop hybrid LGL PS method when it converges to a local minimum. The proposed hybrid feedback PS method is applied to the removal of Geostationary debris to the GEO graveyard region using solar radiation pressure (SRP) and impulsive thrusts. Simulations indicate that the GEO debris removal is achieved using the proposed hybrid feedback PS method. The terminal state error of the semi-major axis and eccentricity are reduced to +0.08 km and $-8.04 \cdot 10^{-7}$, respectively, and an amount of 2.73 m/s impulsive thrust is consumed.

Keywords Feedback pseudospectral method · Hybrid optimal control · GEO debris removal · Impulsive thrusts · Solar radiation pressure

1 Introduction

During the last 60 years, satellites have been continually launched into the precious but limited Geostationary Earth Orbit (GEO), and this results in today's crowded geosynchronous region [1]. The latest annual report of the European Space Agency (ESA) showed that the number of the space debris in GEO has overshoot 1000 as of 2018. Among the GEO objects, 70% of them are space debris. Collision probability analysis [2,3] shows that the possibility of collisions between space debris and operational satellites in GEO is over ten thousand times than what has been previously believed. For each active GEO satellite, a collision is expected every 4 years against one debris within the 1 cm Resident Space Object (RSO) catalog, and every 50 years against one from the 20 cm RSO catalog. To mitigate this severe situation, the Space Debris Mitigation Guidelines [4] were published in 2007 by the Inter-Agency Space Debris Coordination Committee (IADC). The guidelines defined the GEO protected region as a set of orbits with inclination between $[-15°, +15°]$, and the altitude within $\pm$ 200 km about the GEO altitude (35786 km). According to the guidelines, the GEO protected region should be protected against space debris generation. This means that GEO debris should be removed to the GEO graveyard region. To do this, a minimal perigee increase of 235 km + $(1000 \cdot C_R \cdot A/m)$ is required. Here, C_R is the solar radiation pressure (SRP) coefficient, and A/m is the area-to-mass ratio (A/m) of the spacecraft. The terminal orbit eccentricity of the GEO debris should be confined within [0, 0.003].

The feasibility of removing a three-axis stabilized GEO satellite into the GEO graveyard region was first demonstrated in reference [5]. A concept called TugSat was proposed in reference [6] to remove an inactive GEO satel-

✉ Hao Mei
hao.mei@mail.utoronto.ca

Christopher J. Damaren
damaren@utias.utoronto.ca

Xingqun Zhan
xqzhan@sjtu.edu.cn

[1] University of Toronto Institute for Aerospace Studies, Toronto, ON M3H 5T6, Canada

[2] Shanghai Jiao Tong University, Shanghai 200240, China

lite weighted over 1000 kg using a solar sail with an area of 800 m^2. Reference [7] proposed a linear control approach of end-of-life GEO satellites removal using a combination of solar sails and impulsive thrusts. Although end-of-life GEO satellites were removed successfully, the solution in [7] is subjected to a terminal state error. This problem was addressed by the authors' subsequent work that proposed a feedback pseudospectral (PS) method [8]. The same authors has also proposed a so-called "iterations of linearization" approach [9] that generates quasi locally optimal solutions to further reduce the computation cost in [8]. In this paper, a hybrid feedback PS method is proposed for the GEO debris removal mission using a combination of SRP and impulsive thrusts. This work extends the feedback PS method proposed in [8] for the hybrid, non-convex, and non-linear system. The terminal state error and the total ΔV of the required impulsive thrusts in [7] are significantly reduced using the proposed control approach.

Pseudospectral methods [10] have been proven very effective in solving non-linear optimal control problems [11]. PS methods approximate the state and control using a basis of Lagrange polynomials, so the time derivative of the states at the collocation points match the local vector field imposed by the dynamic system, while the states between the collocation points can be approximated through polynomial interpolation. In this way, the optimal control problem is converted into a non-linear programming (NLP) problem regarding only the collocation points. PS method varies with the collocation points applied, including the Legendre–Gauss (LG) [12] points, the Legendre–Gauss–Lobatto (LGL) [13,14] points, and the Legendre–Gauss–Radau (LGR) [15] points. Comparisons of these three methods can be found in [16,17].

The PS methods can be implemented both locally [18] or globally [19]. The local implementation breaks the time interval into several subintervals (segments), so the approximation within each segment can be accomplished with lower order polynomials. The segments are usually linked through continuity constraints on the states or control. The global PS method treats the whole time interval as a single segment, and it converges exponentially if the problem has a smooth solution [11]. However, the order of the approximation can be much higher. The local and global PS methods are compared in references [20,21]. The current forms of the PS methods cannot solve hybrid optimal control problems, but the local LGL PS method provides a natural intuition for the solution. That is, by relaxing the state continuity constraints between the segments, the discontinuities between the states on segment boundaries can be viewed as the results of the impulsive control inputs. This paper follows this intuition and proposes a hybrid LGL PS method to solve hybrid optimal control problems.

PS methods are in nature open-loop methods. The literature on feedback PS methods is limited. An example can be found in the references [22,23] which used a sample-and-hold (SaH) implementation that generates the control input in each time period from the sampled states in the previous time interval. Reference [24] enforced a feedback PS method through receding horizon control (RHC), where terminal state solved from the previous horizon is used as the initial state for the next. The optimal control problem within each time horizon is solved using the LGL PS method. Both the two works above and the traditional open-loop PS methods rely on the assumption that the solution provided by the PS methods is globally optimal.

Whether the PS methods admit the globally optimal solution is dependent on the converted NLP problem. The global optimality of the NLP solution can be guaranteed when the problem is convex. However, this cannot be generally assured for non-convex problems. Because the transcribed NLP problems are usually non-convex when the original optimal control problems are non-convex (such as the GEO debris removal studied in this paper), the open-loop PS methods are prone to locally optimal solutions. The local optimality is a serious challenge for the open-loop PS method. A straightforward approach to circumvent this challenge is to provide an appropriate initial guess, i.e., close enough to the global optimum. However, finding an appropriate initial guess for the non-convex non-linear optimal control problem is not easy, since the transcribed NLP problems can contain a large number of local minima, and the open-loop searching may require a large amount of computational time. The second contribution of this paper is a novel concept that drives the solution out of the local minimum through a linear feedback controller.

A general linear approach to solve an optimal hybrid non-linear time-varying problem is to linearize the dynamic system along a nominal trajectory and then obtain a linear time-varying (LTV) system based on which the hybrid linear feedback controllers can be applied. For the hybrid linear feedback controllers to achieve the control objectives, an important condition is that the nominal trajectory should not deviate too far from the desired trajectory. This is because the real-time trajectory ought to be in the vicinity of the nominal trajectory, for the purpose that the LTV system obtained from linearization can validly approximate the non-linear time-varying dynamic system.

Finding an effective nominal trajectory can be problematic for some optimal hybrid non-linear time-varying problems, since there is no general rule to follow and the searching could have to rely on trial and error. The advantage of the open-loop hybrid PS method is that, even though the globally optimal solution is not generated, the locally optimal trajectory generated by the locally optimal solution provides a natural nominal trajectory to linearize about. Using the linearization and the hybrid linear feedback controller, the optimization accuracy can be further improved based on the

locally optimal solution. The open-loop hybrid PS method and the hybrid linear feedback controller make a perfect pair, since the open-loop hybrid PS method provides a natural nominal trajectory for linearization, and in turn using the linearization, the hybrid linear feedback controller stabilizes the open-loop hybrid PS method.

The contributions of this paper are threefold. Firstly, we extend the local LGL PS method to a hybrid LGL PS method by breaking the state continuity constraints between the segments and governing the dynamics of the LGL points on segment boundaries using discrete dynamic equations. Secondly, we propose a hybrid feedback PS method in which a hybrid linear feedback controller is developed to stabilize the open-loop hybrid PS method when it converges to a local minimum. Thirdly, GEO debris are successfully removed to the GEO graveyard region using SRP and impulsive thrusts in conjunction with the proposed hybrid feedback PS method. The terminal state error of the semi-major axis and eccentricity in reference [7] are reduced from +28.64 km to +0.08 km, and from $+7.26 \cdot 10^{-4}$ to $-8.04 \cdot 10^{-7}$, respectively, and the total ΔV of the required impulsive thrusts is significantly reduced from 10.59 m/s to 2.73 m/s.

This paper is organized as follows. Section 2 presents the dynamic model and the system dynamics for the orbital motion of GEO satellites. Section 3 elaborates on the proposed hybrid feedback PS method, and it is utilized to remove GEO debris using SRP and impulsive thrusts in Sect. 4. Section 5 draws conclusions.

2 Spacecraft dynamics and system modeling

2.1 Spacecraft dynamics

This work utilizes the dynamic model proposed in the references [7–9], which is based on the magnitude comparisons of different accelerations exerted on GEO satellites, and the drifts of the classical orbital elements due to each perturbative term over the satellites' removal time. To generate general GEO debris removal results that are independent of the mass of GEO satellites, the dynamic model is built upon the accelerations rather than the forces exerted on GEO satellites. The total acceleration exerted on a GEO satellite can be described as $\ddot{\boldsymbol{r}} = \ddot{\boldsymbol{r}}_{\oplus} + \ddot{\boldsymbol{r}}_3 + \ddot{\boldsymbol{r}}_{\boldsymbol{SRP}}$. Here, $\ddot{\boldsymbol{r}}_{\oplus}$ is the Earth's gravitational acceleration, including the two-body gravitational acceleration and the Earth's gravitational perturbations, $\ddot{\boldsymbol{r}}_3$ is the third-body (the Sun and Moon) gravitational perturbation, and $\ddot{\boldsymbol{r}}_{\boldsymbol{SRP}}$ denotes the acceleration caused by SRP which can be controlled by the solar sail control angles.

SRP is caused by the photons emitted by the Sun. For an ideal solar sail, all the incoming photons from the Sun are reflected. The acceleration due to SRP is caused by the reflection of the photons, and it is given as [25]

$$\ddot{\boldsymbol{r}}_{\boldsymbol{SRP}} = \left(2P_{\odot}\frac{A}{m}\cos^2\alpha\right)\hat{\boldsymbol{n}}. \tag{1}$$

Here, $P_{\odot}$ is the magnitude of SRP. Around the Earth, $P_{\odot}$ at 1 AU ($1.496 \cdot 10^8$ km) from the Sun is equal to $4.56 \cdot 10^{-6}$ N/m^2. The quantity A/m is the area-to-mass ratio of the spacecraft. The control angle α ($\alpha \in [0°, 90°]$) is the cone angle (the pitch angle in the 2D case) of the solar sail, which is the angle between the sail normal vector $\hat{\boldsymbol{n}}$ and the Sun-line vector $\hat{\boldsymbol{u}}$ (Fig. 1b). The eclipse by the Earth is considered in this work, and it is detailed in references [7–9].

Earth's gravitational potential is given by [26]

$$\begin{aligned} U = {} & \frac{\mu_{\oplus}}{r} - \frac{\mu_{\oplus}}{r}\sum_{l=2}^{\infty} J_l \left(\frac{R_{\oplus}}{r}\right)^l P_l(\sin\phi) \\ & + \frac{\mu_{\oplus}}{r}\sum_{l=2}^{\infty}\sum_{m=1}^{l}\left(\frac{R_{\oplus}}{r}\right)^l P_{l,m}(\sin\phi) \\ & \left\{C_{l,m}\cos(m\lambda_{sat}) + S_{l,m}\sin(m\lambda_{sat})\right\}. \end{aligned} \tag{2}$$

Here, $\mu_{\oplus}$ is the Earth's gravitational parameter, r is the distance of the satellite from the Earth, ϕ and λ are the latitude and longitude of satellite, P_l ($P_{l,m}$) denote the conventional (associated) Legendre polynomials, and J_l ($C_{l,m}$, $S_{l,m}$) are the zonal (sectoral and tesseral) harmonics. Earth's gravitational acceleration in the Earth Centered Earth Fixed (ECEF) frame can be obtained by taking the gradient of the total gravitational potential. As in [7], this work uses the second- and the third-order terms of the Earth's gravitational perturbation in the dynamic model.

The equation of motion of a three-body system is given by [26]

$$\ddot{\boldsymbol{r}}_{\oplus sat} = -\frac{\mu_{\oplus}\boldsymbol{r}_{\oplus sat}}{r_{\oplus sat}^3} + \mu_3\left(\frac{\boldsymbol{r}_{sat3}}{r_{sat3}^3} - \frac{\boldsymbol{r}_{\oplus 3}}{r_{\oplus 3}^3}\right). \tag{3}$$

Here, μ_3 is the third-body's gravitational parameter. By expanding the term $\frac{\boldsymbol{r}_{sat3}}{r_{sat3}^3}$ in Eq. (3) using Legendre polynomials, Eq. (3) becomes

$$\ddot{\boldsymbol{r}}_{\oplus sat} = -\frac{\mu_{\oplus}\boldsymbol{r}_{\oplus sat}}{r_{\oplus sat}^3} - \mu_3\left(\frac{-\boldsymbol{r}_{sat3}(3B + 3B^2 + B^3) + \boldsymbol{r}_{\oplus sat}}{r_{\oplus 3}^3}\right), \tag{4}$$

where

$$B = \sum_{j=1}^{\infty} P_j[\cos\varsigma]\left(\frac{r_{\oplus sat}}{r_{\oplus 3}}\right)^j. \tag{5}$$

Here, ς is the angle between $\boldsymbol{r}_{\oplus 3}$ and $\boldsymbol{r}_{\oplus sat}$. Equation (5) can be partitioned as $B = B_1 + B_2 + B_3 + \cdots$. As in [7], this work utilizes the following dynamic model for the third-body gravitational accelerations. For the Sun, the B_1 and B_2 terms are applied. For the Moon, the B_1, B_2 and B_3 terms are applied when $A/m \geq 0.1$ m^2/kg, while the B_4 and B_5 terms are also considered when $A/m \geq 0.001$ m^2/kg.

2.2 Dynamic system modeling

This work takes the classical orbital elements $\boldsymbol{x} = [a\ e\ i\ \omega\ \Omega\ \theta]^{\mathrm{T}}$ as the state. The time derivative of the state is given by [26]

$$\dot{\boldsymbol{x}}(t) = \boldsymbol{P}(x)\boldsymbol{f}_t + \boldsymbol{b}(x), \tag{6}$$

where

$$\boldsymbol{P}(x) = \begin{pmatrix} \frac{2a^2}{\sqrt{\mu_\oplus a(1-e^2)}} e\sin(\theta) & \frac{2a^2}{\sqrt{\mu_\oplus a(1-e^2)}}(1+e\cos(\theta)) & 0 \\ \sqrt{\frac{a(1-e^2)}{\mu_\oplus}}\sin(\theta) & \sqrt{\frac{a(1-e^2)}{\mu_\oplus}}\frac{2\cos(\theta)+e(1+\cos^2(\theta))}{1+e\cos(\theta)} & 0 \\ 0 & 0 & \sqrt{\frac{a(1-e^2)}{\mu_\oplus}}\frac{\cos(\omega+\theta)}{1+e\cos(\theta)} \\ -\sqrt{\frac{a(1-e^2)}{\mu_\oplus}}\frac{\cos(\theta)}{e} & \sqrt{\frac{a(1-e^2)}{\mu_\oplus}}\frac{(2+e\cos(\theta))\sin(\theta)}{e(1+e\cos(\theta))} & -\sqrt{\frac{a(1-e^2)}{\mu_\oplus}}\frac{\sin(\omega+\theta)}{\tan(i)(1+e\cos(\theta))} \\ 0 & 0 & \sqrt{\frac{a(1-e^2)}{\mu_\oplus}}\frac{\sin(\omega+\theta)}{\sin(i)(1+e\cos(\theta))} \\ \sqrt{\frac{a(1-e^2)}{\mu_\oplus}}\frac{\cos(\theta)}{e} & -\sqrt{\frac{a(1-e^2)}{\mu_\oplus}}\frac{(2+e\cos(\theta))\sin(\theta)}{e(1+e\cos(\theta))} & 0 \end{pmatrix}, \tag{7}$$

and

$$\boldsymbol{b}(x) = \begin{pmatrix} 0 \\ 0 \\ 0 \\ 0 \\ 0 \\ \sqrt{\frac{\mu_\oplus}{a^3}}\frac{(1+e\cos(\theta))^2}{\sqrt{(1-e^2)^3}} \end{pmatrix}. \tag{8}$$

In Eqs. (6)–(8), $\boldsymbol{f}_t = [f_r,\ f_\theta,\ f_z]^{\mathrm{T}}$ are the perturbative accelerations expressed in the Local-Vertical Local-Horizontal (LVLH, denoted as $\mathcal{F}_o$) frame, and $\mu_\oplus$ is the Earth's gravitational parameter.

To express the acceleration caused by SRP, a solar sail frame $\mathcal{F}_s$ is constructed. As depicted in Fig. 1 (a), axis $\hat{\boldsymbol{s}}_1$ is along the direction of the Sun-line vector (which points from the Sun to the satellite) $\hat{\boldsymbol{u}}$, axis $\hat{\boldsymbol{s}}_3$ lies in the plane constructed by $\hat{\boldsymbol{s}}_1$ and $\hat{\boldsymbol{g}}_3$ (with $\mathcal{F}_g$ being the ECI frame) and being perpendicular to $\hat{\boldsymbol{s}}_1$. Axis $\hat{\boldsymbol{s}}_2$ completes the right-hand rule. In the solar sail frame $\mathcal{F}_s$, from Fig. 1 (b), the sail normal vector $\hat{\boldsymbol{n}}$ in $\mathcal{F}_s$ can be expressed as

$$\hat{\boldsymbol{n}}_s = [\cos\alpha,\ \sin(\alpha)\sin(\delta),\ \sin(\alpha)\cos(\delta)]^{\mathrm{T}}, \tag{9}$$

where α ($\in [0°, 90°]$) and δ ($\in [0°, 360°]$) are the cone angle and clock angle of the solar sail, respectively. The rotation matrix from the solar sail frame ($\mathcal{F}_s$) to the Earth Centered Inertial (ECI) frame ($\mathcal{F}_g$) can be calculated as $\boldsymbol{C}_{GS} = \boldsymbol{f}_g \cdot \boldsymbol{f}_s^{\mathrm{T}}$, in which $\boldsymbol{f}_g$ is the vectrix [27] defined as $\boldsymbol{f}_g = (\hat{\boldsymbol{g}}_1,\ \hat{\boldsymbol{g}}_2,\ \hat{\boldsymbol{g}}_3)^{\mathrm{T}}$, and similarly, $\boldsymbol{f}_s = (\hat{\boldsymbol{s}}_1,\ \hat{\boldsymbol{s}}_2,\ \hat{\boldsymbol{s}}_3)^{\mathrm{T}}$. Combining Eq. (1), the acceleration caused by SRP in the solar sail frame ($\mathcal{F}_s$) is equal to $2P_\odot \cdot (A/m) \cdot \cos^2(\alpha) \cdot \hat{\boldsymbol{n}}$; thus, the acceleration caused by SRP in the LVLH frame ($\mathcal{F}_o$) can be expressed as

$$\begin{aligned} \boldsymbol{f}_{SRP}(\boldsymbol{x}, \boldsymbol{u}) &= 2P_\odot \cdot A/m \cdot \cos^2(\alpha) \\ &\quad \cdot \boldsymbol{C}_{OP}(\boldsymbol{x})\boldsymbol{C}_{PG}(\boldsymbol{x})\boldsymbol{C}_{GS}(t) \cdot \hat{\boldsymbol{n}}_s. \end{aligned} \tag{10}$$

Here, $\boldsymbol{C}_{OP}(\boldsymbol{x}) = \boldsymbol{C}_3(\theta)$, $\boldsymbol{C}_{PG}(\boldsymbol{x}) = \boldsymbol{C}_3(\omega)\boldsymbol{C}_1(i)\boldsymbol{C}_3(\Omega)$ are the rotation matrices from the perifocal frame ($\mathcal{F}_p$) to the LVLH frame ($\mathcal{F}_o$) and from the ECI frame ($\mathcal{F}_g$) to the perifocal frame ($\mathcal{F}_p$), respectively. Taking the two-body acceleration and the disturbance accelerations into account, we have

$$\dot{\boldsymbol{x}}(t) = \boldsymbol{f}_c(\boldsymbol{x}, \boldsymbol{u}, t) \triangleq \boldsymbol{P}(\boldsymbol{x}) \cdot \boldsymbol{f}_{SRP}(\boldsymbol{x}, \boldsymbol{u}) + \boldsymbol{b}(\boldsymbol{x}) + \boldsymbol{d}(t). \tag{11}$$

Here, $\boldsymbol{P}(\boldsymbol{x}) \cdot \boldsymbol{f}_{SRP}(\boldsymbol{x}, \boldsymbol{u})$ is the time derivative of the state due to SRP, in which the sail normal vector $\hat{\boldsymbol{n}}_s$ in $\boldsymbol{f}_{SRP}(\boldsymbol{x}, \boldsymbol{u})$ is determined by the solar sail control angles α and δ. The column $\boldsymbol{b}(\boldsymbol{x})$ is defined in Eq. (8), and it is the time derivative of the true anomaly due to the two-body acceleration. The quantity $\boldsymbol{d}(t) = \boldsymbol{P}(\boldsymbol{x}(t)) \cdot \boldsymbol{a}_d(t)$ is the disturbance to the dynamic system, in which $\boldsymbol{a}_d(t)$ is the perturbative acceleration expressed in the LVLH frame ($\mathcal{F}_o$). Note that in this work, the disturbance acceleration is approximated and modeled as a function only of time. This approximation is valid when the real-time state trajectory is close to the nominal state trajectory along which the disturbance is modeled.

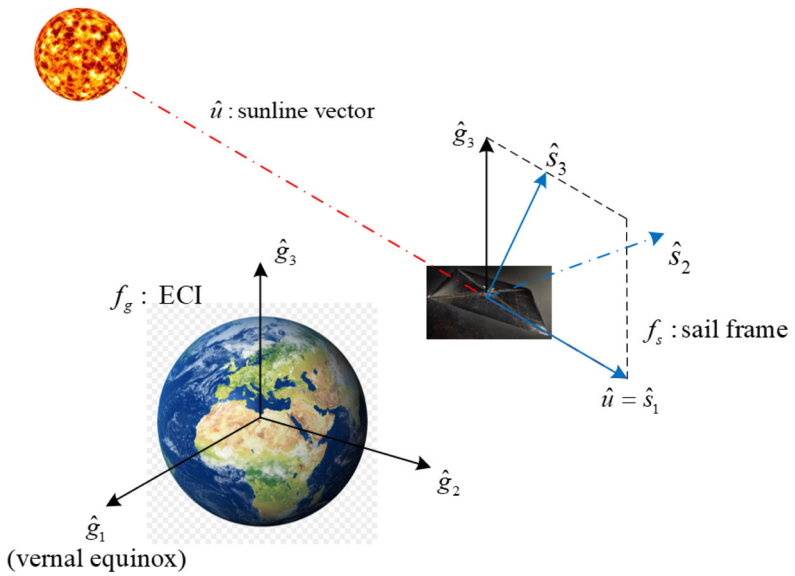

(a) The $\mathcal{F}_s$ Frame

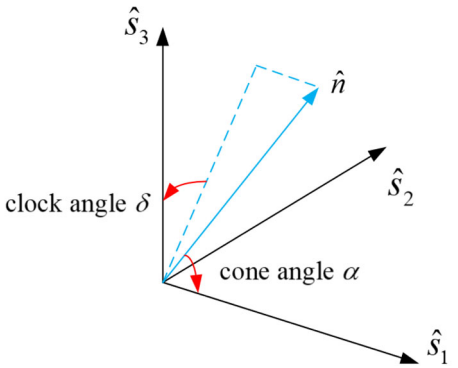

(b) Cone Angle and Clock Angle in $\mathcal{F}_s$

Fig. 1 Express SRP in the constructed frame $\mathcal{F}_s$

2.3 Equation of motion under an impulsive thrust

Consider an impulsive thrust applied at time epoch t_k

$$\dot{\boldsymbol{x}}(t) = \boldsymbol{P}(\boldsymbol{x})\cdot\boldsymbol{f}_{SRP}(\boldsymbol{x},\boldsymbol{u})+\boldsymbol{b}(\boldsymbol{x})+\boldsymbol{d}(t)+\boldsymbol{P}(\boldsymbol{x})\boldsymbol{v}(t_k)\cdot\delta_D(t-t_k). \quad (12)$$

Here, $\boldsymbol{v}(t_k)$ is the thrust vector expressed in the LVLH frame ($\mathcal{F}_o$). The function $\delta_D(t)$ is the Dirac function defined as $\delta_D(t) = 0\ (t \neq 0)$, $\delta_D(t) = +\infty\ (t = 0)$ and $\int_{-\infty}^{+\infty}\delta_D(t) = 1$. Note that the first three terms on the right-hand side of Eq. (12) are continuous in time. By integrating Eq. (12) from time epoch t_k^- to t_k^+, we have

$$\int_{t_k^-}^{t_k^+}\dot{\boldsymbol{x}}(t)dt = \int_{t_k^-}^{t_k^+}\boldsymbol{P}(\boldsymbol{x})\boldsymbol{v}(t_k)\cdot\delta_D(t-t_k)dt, \quad (13)$$

which results in

$$\boldsymbol{x}(t_k^+) \triangleq \boldsymbol{f}_d(\boldsymbol{x}(t_k^-),\boldsymbol{v}(t_k)) = \boldsymbol{x}(t_k^-) + \boldsymbol{P}(\boldsymbol{x}_{t_k^-})\boldsymbol{v}(t_k). \quad (14)$$

Here, $\boldsymbol{P}(\boldsymbol{x}_{t_k^-})$ denotes the $\boldsymbol{P}(\boldsymbol{x})$ matrix at the time epoch t_k, and $\boldsymbol{v}(t_k)$ is the impulsive thrust applied at t_k expressed in the LVLH frame ($\mathcal{F}_o$). In this work, we consider the accelerations (not forces) exerted on the GEO spacecraft. Thus, the unit of the impulse $v(t_k)$ is m/s.

3 Hybrid feedback pseudospectral method

In Sect. 3.1, the local Legendre–Gauss–Lobatto (LGL) PS method is first extended to a hybrid LGL PS method which is capable of solving hybrid non-linear optimal control problems. Sections 3.2, 3.3 and 3.4 elaborate on the proposed hybrid feedback PS method, in which a hybrid linear feed-

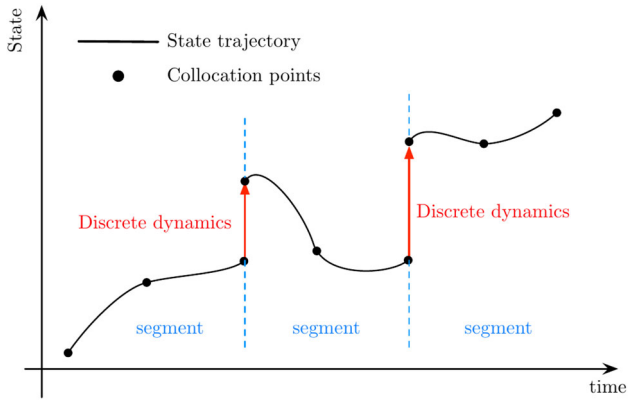

Fig. 2 General description of the hybrid LGL PS method

back controller is developed to stabilize the open-loop hybrid LGL PS method when it converges to a local minimum.

3.1 Hybrid Legendre–Gauss–Lobatto pseudospectral method

Figure 2 generally describes the proposed hybrid LGL PS method. The basic idea of this method is to approximate the state and the continuous control using polynomials that interpolate their values at the LGL collocation points, and govern the dynamics of the LGL points on the segment boundaries using discrete dynamic equations.

A general hybrid optimal control problem is formulated as follows. Determine the state-control group $\{\boldsymbol{x} \in \mathbb{R}^{N_x}, \boldsymbol{u} \in \mathbb{R}^{N_u}, \boldsymbol{v} \in \mathbb{R}^{N_v}\}$, that minimizes the hybrid cost functional

$$\begin{aligned}\mathcal{J} = \phi[\boldsymbol{x}(t_f), t_f] + \sum_{k=1}^{M} \int_{t_{k-1}^+}^{t_k^-} \mathcal{L}(\boldsymbol{x}(t), \boldsymbol{u}(t), t)dt \\ + \sum_{k=1}^{M-1} \mathcal{M}(\boldsymbol{x}(t_k^-), \boldsymbol{v}(t_k), t_k),\end{aligned} \tag{15}$$

subject to

$$\dot{\boldsymbol{x}}(t) = \boldsymbol{f}(\boldsymbol{x}(t), \boldsymbol{u}(t), t), \ t \neq t_k, \tag{16}$$

$$\boldsymbol{x}(t_k^+) = \boldsymbol{g}(\boldsymbol{x}(t_k^-), \boldsymbol{v}(t_k), t_k), \ t = t_k, \tag{17}$$

$$\boldsymbol{C}_c(\boldsymbol{x}, \boldsymbol{u}, t) = \boldsymbol{0}, \tag{18}$$

$$\boldsymbol{C}_d(\boldsymbol{x}(t_k^-), \boldsymbol{v}(t_k), t_k) = \boldsymbol{0}, \ t = t_k, \tag{19}$$

$$\boldsymbol{H}_c(\boldsymbol{x}, \boldsymbol{u}, t) \leq \boldsymbol{0}, \tag{20}$$

$$\boldsymbol{H}_d(\boldsymbol{x}(t_k^-), \boldsymbol{v}(t_k), t_k) \leq \boldsymbol{0}, \ t = t_k, \tag{21}$$

$$\boldsymbol{E}(\boldsymbol{x}(t_0), \boldsymbol{x}(t_f), t_0, t_f) = \boldsymbol{0}. \tag{22}$$

Here, $t_0^+ = t_0$, $t_M^- = t_f$, and t_k $(k = 1, ..., M-1)$ represents the $M-1$ prescribed impulse time epochs. In Eq. (15), the functions ϕ, $\mathcal{L}$ and $\mathcal{M}$ are the terminal, continuous, and discrete cost functions, respectively. The functions $\boldsymbol{f} : \mathbb{R}^{N_x} \times \mathbb{R}^{N_u} \times \mathbb{R} \to \mathbb{R}^{N_x}$, $\boldsymbol{g} : \mathbb{R}^{N_x} \times \mathbb{R}^{N_v} \times \mathbb{R} \to \mathbb{R}^{N_x}$ are the continuous and discrete system dynamic constraints, respectively. The functions $\boldsymbol{C}_c : \mathbb{R}^{N_x} \times \mathbb{R}^{N_u} \times \mathbb{R} \to \mathbb{R}^{N_{cc}}$, $\boldsymbol{H}_c : \mathbb{R}^{N_x} \times \mathbb{R}^{N_u} \times \mathbb{R} \to \mathbb{R}^{N_{hc}}$ are the continuous equality and inequality constraints. The functions $\boldsymbol{C}_d : \mathbb{R}^{N_x} \times \mathbb{R}^{N_v} \times \mathbb{R} \to \mathbb{R}^{N_{cd}}$, $\boldsymbol{H}_d : \mathbb{R}^{N_x} \times \mathbb{R}^{N_v} \times \mathbb{R} \to \mathbb{R}^{N_{hd}}$ are the discrete equality and inequality constraints, and $\boldsymbol{E} : \mathbb{R}^{N_x} \times \mathbb{R}^{N_x} \times \mathbb{R} \times \mathbb{R} \to \mathbb{R}^{N_e}$ represents the boundary conditions. Here, we propose a hybrid LGL PS method that transforms the general hybrid optimal control problem given by Eqs. (15)–(22) into an NLP problem.

First, the original time interval $I = [t_0, \ t_f]$ is divided into M subintervals I_k $(k = 1, ..., M)$, such that $I_k = [t_{k-1}, \ t_k]$ and $\bigcup_{i=1}^{M} I_k = I$. The boundaries of the subintervals are selected as the $M-1$ impulse time epochs t_k $(k = 1, ..., M-1)$, together with the initial and terminal time t_0 and t_f. For each subinterval I_k, the time span in I_k (denoted as $t^{(k)}$, $t_{k-1} \leq t^{(k)} \leq t_k$) is transformed into $\tau = [-1, \ 1]$ via the affine transformation

$$\tau = \frac{2t^{(k)}}{t_k - t_{k-1}} - \frac{t_k + t_{k-1}}{t_k - t_{k-1}}. \tag{23}$$

The state and the continuous control in each subinterval I_k are approximated using a basis of $N+1$ Lagrange polynomials $L_i(\tau)$ $(i = 0, ..., N)$:

$$\boldsymbol{x}^{(k)}(\tau) = \sum_{i=0}^{N} \boldsymbol{X}_i^{(k)} L_i(\tau), \tag{24}$$

$$\boldsymbol{u}^{(k)}(\tau) = \sum_{i=0}^{N} \boldsymbol{U}_i^{(k)} L_i(\tau), \tag{25}$$

where $\boldsymbol{X}_i^{(k)}$ and $\boldsymbol{U}_i^{(k)}$ are the coordinates of the state and continuous control under the Lagrange polynomial basis $L_i(\tau)$ in the subinterval I_k. The LGL collocation points are distributed over the interval $[-1, \ 1]$ and are given as $t_0 = -1$, $t_N = 1$, and t_l $(1 \leq l \leq N-1)$ are the zeros of $\dot{L}_N$. By differentiating Eq. (24) and evaluating at the jth collocation point, we have

$$\dot{\boldsymbol{x}}^{(k)}(\tau_j) = \sum_{i=0}^{N} \boldsymbol{X}_i^{(k)} \dot{L}_i(\tau_j) = \sum_{i=0}^{N} D_{ji} \boldsymbol{X}_i^{(k)}(\tau_j). \tag{26}$$

The state derivatives at the collocation points should match the local vector fields imposed by Eq. (16), and the dynamics of the LGL points on segment boundaries are governed by the discrete dynamic equation [Eq. (17)], thus

$$\boldsymbol{D}\boldsymbol{X}_{0:N}^{(k)} = \left(\frac{t_k - t_{k-1}}{2}\right) \boldsymbol{F}(\boldsymbol{X}_{0:N}^{(k)}, \boldsymbol{U}_{0:N}^{(k)}, t^{(k)}(\boldsymbol{\tau}_{0:N})), \tag{27}$$

$$\boldsymbol{x}^{(k+1)}(\tau_0) = \sum_{i=0}^{N} \boldsymbol{X}_i^{(k+1)} L_i(\tau_0) = \boldsymbol{G}(\boldsymbol{X}_N^{(k)}, \boldsymbol{v}^{(k)}(t^{(k)}(\tau_N))), t^{(k)}(\tau_N)). \tag{28}$$

Here, the $(N+1) \times (N+1)$ square matrix $\boldsymbol{D}$ is the Lobatto PS differentiation matrix. The column matrix $\boldsymbol{X}_N^{(k)}$ $(k = 1, ..., M-1)$, the $(N+1)$th column of $\boldsymbol{X}_{0:N}^{(k)}$, represents the coordinate of the state under the basis $L_i(\tau)$ before the kth impulse, and $\boldsymbol{x}^{(k+1)}(\tau_0)$ is the state after the kth impulse. Note that the ith column $(i = 0, 1, ..., N)$ of $\boldsymbol{X}_{0:N}^{(k)}$ represents the coordinate of the state under the basis $L_i(\tau)$ at the ith collocation point in the kth subinterval.

Now, the NLP problem obtained from transcribing the hybrid optimal control problem given in Eqs. (15)–(22) can be written in the following manner. Minimize

$$\mathcal{J} = \phi[\boldsymbol{X}_N^{(M)}, t_f] + \sum_{k=1}^{M} \left(\frac{t_k - t_{k-1}}{2}\right) \sum_{i=0}^{N} \omega_i \mathcal{L}(\boldsymbol{X}_i^{(k)}, \boldsymbol{U}_i^{(k)}, t^{(k)}(\tau_i)) + \sum_{k=1}^{M-1} \mathcal{M}(\boldsymbol{X}_N^{(k)}, \boldsymbol{v}^{(k)}(t^{(k)}(\tau_N))), t^{(k)}(\tau_N)), \tag{29}$$

subject to

$$\boldsymbol{D}\boldsymbol{X}_{0:N}^{(k)} - \left(\frac{t_k - t_{k-1}}{2}\right) \boldsymbol{F}(\boldsymbol{X}_{0:N}^{(k)}, \boldsymbol{U}_{0:N}^{(k)}, t^{(k)}(\boldsymbol{\tau}_{0:N})) = \boldsymbol{0}, \tag{30}$$

$$\sum_{i=0}^{N} \boldsymbol{X}_i^{(k+1)} L_i(\tau_0) - \boldsymbol{G}(\boldsymbol{X}_N^{(k)}, \boldsymbol{v}^{(k)}(t^{(k)}(\tau_N))), t^{(k)}(\tau_N)) = \boldsymbol{0}, \tag{31}$$

$$\boldsymbol{C}_c(\boldsymbol{X}_{0:N}^{(k)}, \boldsymbol{U}_{0:N}^{(k)}, t^{(k)}(\boldsymbol{\tau}_{0:N})) = \boldsymbol{0}, \tag{32}$$

$$\boldsymbol{C}_d(\boldsymbol{X}_N^{(k)}, \boldsymbol{v}^{(k)}(t^{(k)}(\tau_N))), t^{(k)}(\tau_N)) = \boldsymbol{0}, \tag{33}$$

$$\boldsymbol{H}_c(\boldsymbol{X}_{0:N}^{(k)}, \boldsymbol{U}_{0:N}^{(k)}, t^{(k)}(\boldsymbol{\tau}_{0:N})) \leq \boldsymbol{0}, \tag{34}$$

$$\boldsymbol{H}_d(\boldsymbol{X}_N^{(k)}, \boldsymbol{v}^{(k)}(t^{(k)}(\tau_N))), t^{(k)}(\tau_N)) \leq \boldsymbol{0}, \tag{35}$$

$$\boldsymbol{E}(\boldsymbol{X}_0^{(k)}, \boldsymbol{X}_N^{(k)}, t^{(k)}(\tau_0), t^{(k)}(\tau_N)) = \boldsymbol{0}. \tag{36}$$

For Eqs. (29), (30), (32), (34), and (36), k $(k = 1, 2..., M)$ denotes the kth subinterval. For Eqs. (31), (33), and (35), k $(k = 1, 2..., M-1)$ denotes the kth impulsive. The quantities ω_i $(i = 0, 1, ..., N)$ in Eq. (29) are the LGL weights and are given as

$$\omega_i = \frac{2}{N(N+1)} \frac{1}{[L_N(t_i)]^2}, \qquad i = 0, 1, ..., N. \tag{37}$$

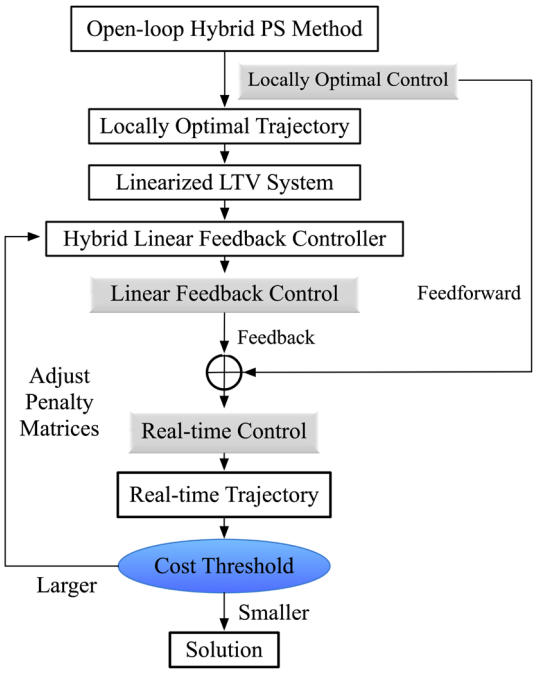

Fig. 3 General description of the hybrid feedback PS method

3.2 Hybrid feedback pseudospectral method

In the open-loop hybrid LGL PS method, the initial guess is an important factor. An inappropriate initial guess can cause the solution to be trapped at a local minimum. Finding an effective initial guess for the open-loop hybrid LGL PS method is a challenging problem, especially when solving complex non-convex non-linear optimal control problems. This is because when the transcribed NLP problem contains a large number of local minima, the open-loop search of an effective initial guess could cost a large computational time. This deficiency is serious, since PS methods are open-loop methods.

This paper uses feedback approaches to tackle this problem. The concept is illustrated in Fig. 3. When the open-loop hybrid PS method converges to a local minimum, the dynamic system is linearized along the locally optimal state trajectory (called the nominal state trajectory) and a hybrid linear feedback controller is designed. If the open-loop hybrid PS solution is a locally optimal solution, the cost function can be further reduced using the hybrid linear feedback controller. The real-time control is the addition of the feedforward control generated by the open-loop hybrid PS method, and the feedback control obtained from the hybrid linear feedback controller. The penalty matrices in the hybrid linear feedback controller need to be chosen subtly and judiciously, so that the desired optimization accuracy can be achieved. The solution is finalized when the cost function is within a threshold.

3.3 Hybrid linear feedback controller

Consider the continuous dynamic system in Eq. (11), $\dot{\boldsymbol{x}}(t) = \boldsymbol{f}_c(\boldsymbol{x}(t), \boldsymbol{u}(t), t)$, where $\boldsymbol{u} = [\alpha,\ \delta]^{\mathrm{T}}$. Let $\{\boldsymbol{x}_n(t),\ \boldsymbol{u}_n(t),\ \boldsymbol{v}_n(t_k),\ \boldsymbol{d}_n(t)\}$ $(k = 1, ..., M-1)$ be the locally optimal state trajectory generated by the open-loop hybrid LGL PS method. By linearizing the continuous dynamic system along the locally optimal state trajectory, we have

$$\delta\dot{\boldsymbol{x}} = \underbrace{\frac{\partial \boldsymbol{f}_c}{\partial \boldsymbol{x}}[\boldsymbol{x}_n, \boldsymbol{u}_n, t]}_{\text{denote as } \boldsymbol{A}(t)}\delta\boldsymbol{x}(t) + \underbrace{\frac{\partial \boldsymbol{f}_c}{\partial \boldsymbol{u}}[\boldsymbol{x}_n, \boldsymbol{u}_n, t]}_{\text{denote as } \boldsymbol{B}(t)}\delta\boldsymbol{u}(t). \tag{38}$$

Equation (38) is a first-order approximation of the error dynamics. In Eq. (38), $\delta\boldsymbol{x}(t) \approx \boldsymbol{x}(t) - \boldsymbol{x}_n(t)$, $\delta\boldsymbol{u}(t) \approx \boldsymbol{u}(t) - \boldsymbol{u}_n(t)$ are deviations from the nominal trajectory and nominal control input, respectively. Let $\boldsymbol{X}(t) \triangleq \delta\boldsymbol{x}(t)$ be the state of the linearized dynamic system, and $\boldsymbol{U}(t) \triangleq \delta\boldsymbol{u}(t)$ be the control of the linearized dynamic system, then Eq. (38) can be written as

$$\dot{\boldsymbol{X}}(t) = \boldsymbol{A}(t)\boldsymbol{X}(t) + \boldsymbol{B}(t)\boldsymbol{U}(t). \tag{39}$$

This is a linear time-varying (LTV) dynamic system. The system matrix $\boldsymbol{A}(t)$ and the control matrix $\boldsymbol{B}(t)$ are modeled along the nominal trajectory $\{\boldsymbol{x}_n(t), \boldsymbol{u}_n(t), \boldsymbol{v}_n(t_k), \boldsymbol{d}_n(t)\}$. Note that the nominal trajectory is discontinuous due to the impulses. When discontinuity occurs, $\boldsymbol{x}_n(t_k^+) = \boldsymbol{x}_n(t_k^-) + \boldsymbol{P}(\boldsymbol{x}_{t_k})\boldsymbol{v}_n(t_k)$. Combining $\boldsymbol{X}(t_k^{\pm}) = \boldsymbol{x}(t_k^{\pm}) - \boldsymbol{x}_n(t_k^{\pm})$, the discrete dynamic equation in Eq. (14) becomes

$$\boldsymbol{X}(t_k^+) = \boldsymbol{X}(t_k^-) + \boldsymbol{P}(\boldsymbol{x}_{t_k})\boldsymbol{V}(t_k). \tag{40}$$

Here, $\boldsymbol{V}(t_k) = \boldsymbol{v}(t_k) - \boldsymbol{v}_n(t_k)$ denotes the deviation of the real-time impulse $\boldsymbol{v}(t_k)$ from the nominal impulse $\boldsymbol{v}_n(t_k)$ at the time epoch t_k.

If the state $\boldsymbol{X}(t) \approx \boldsymbol{x}(t) - \boldsymbol{x}_n(t)$ in the linearized dynamic system (Eqs. (39)) is equal to the desired state $\boldsymbol{Z}(t)$ defined as $\boldsymbol{Z}(t) \triangleq \boldsymbol{x}_d(t) - \boldsymbol{x}_n(t)$, then $\boldsymbol{x}(t) \approx \boldsymbol{x}_d(t)$, which is the desired situation. Here, $\boldsymbol{x}(t)$ is approximately equal to $\boldsymbol{x}_d(t)$, because the linear state $\boldsymbol{X}(t)$ is a first-order approximation. This recovers the control objective and gives rise to a hybrid tracking problem. The goal of this hybrid tracking problem is to minimize the hybrid cost functional (for completeness, we rewrite the discrete dynamic system into the complete form $\boldsymbol{X}(t_k^+) = \boldsymbol{C}_k\boldsymbol{X}(t_k^-) + \boldsymbol{D}_k\boldsymbol{V}(t_k)$. In this section, $\boldsymbol{C}_k = \boldsymbol{I}_6$, $\boldsymbol{D}_k = \boldsymbol{P}(\boldsymbol{x}_{t_k})$)

$$\begin{aligned}\mathcal{J}(\boldsymbol{X}(t), \boldsymbol{Z}(t), \boldsymbol{U}(t), \boldsymbol{V}(t_k)) &= \frac{1}{2}\boldsymbol{e}^T(t_f)\boldsymbol{S}\boldsymbol{e}(t_f) \\ &+ \sum_{k=1}^{M}\int_{t_{k-1}^+}^{t_k^-}\left(\frac{1}{2}\boldsymbol{e}^T(t)\boldsymbol{Q}\boldsymbol{e}(t) + \frac{1}{2}\boldsymbol{U}^T(t)\boldsymbol{R}\boldsymbol{U}(t)\right)dt \\ &+ \sum_{k=1}^{M-1}\left(\frac{1}{2}\boldsymbol{e}^T(t_k^-)\boldsymbol{Q}_k\boldsymbol{e}(t_k^-) + \frac{1}{2}\boldsymbol{V}^T(t_k)\boldsymbol{R}_k\boldsymbol{V}(t_k)\right),\end{aligned} \tag{41}$$

where $\boldsymbol{e}(t) = \boldsymbol{X}(t) - \boldsymbol{Z}(t)$ is the tracking error. The matrices $\boldsymbol{S} = \boldsymbol{S}^T \geq 0$ penalize the terminal state error, $\boldsymbol{Q} = \boldsymbol{Q}^T \geq 0$, $\boldsymbol{R} = \boldsymbol{R}^T > 0$ penalize the continuous-time tracking error and control inputs, and $\boldsymbol{Q}_k = \boldsymbol{Q}_k^T \geq 0$, $\boldsymbol{R}_k = \boldsymbol{R}_k^T > 0$ set the discrete-time tracking error and control penalties. The epochs t_k $(k = 1, 2..., M-1)$ represent the $M-1$ prescribed time instances when the impulsive thrusts are applied. The solutions of this hybrid tracking problem can be found in Eqs. (51) and (57) of reference [7] with the disturbance term being zero, which are given by

$$\boldsymbol{U}^*(t) = -\boldsymbol{R}^{-1}\boldsymbol{B}^T(t)\left(\boldsymbol{G}(t)\boldsymbol{X}(t) - \boldsymbol{g}(t)\right), \tag{42}$$

$$\begin{aligned}\boldsymbol{V}^*(t_k) = -\boldsymbol{R}_k^{-1}\boldsymbol{D}_k^T\boldsymbol{C}_k^{-T}\big((\boldsymbol{G}(t_k^-) \\ -\boldsymbol{Q}_k)\boldsymbol{X}(t_k^-) - \boldsymbol{g}(t_k^-) + \boldsymbol{Q}_k\boldsymbol{Z}(t_k)\big),\end{aligned} \tag{43}$$

in which $\boldsymbol{G}(t)$ and $\boldsymbol{g}(t)$ can be calculated by integrating the following equations simultaneously backward:

$$\begin{aligned}\dot{\boldsymbol{G}}(t) = &-\boldsymbol{Q} - \boldsymbol{A}^T(t)\boldsymbol{G}(t) - \boldsymbol{G}(t)\boldsymbol{A}(t) \\ &+\boldsymbol{G}(t)\boldsymbol{B}(t)\boldsymbol{R}^{-1}\boldsymbol{B}^T(t)\boldsymbol{G}(t),\end{aligned} \tag{44}$$

$$\begin{aligned}\dot{\boldsymbol{g}}(t) = &-\boldsymbol{Q}\boldsymbol{Z}(t) - \Big(\boldsymbol{A}^T(t) \\ &-\boldsymbol{G}(t)\boldsymbol{B}(t)\boldsymbol{R}^{-1}\boldsymbol{B}^T(t)\Big)\boldsymbol{g}(t),\end{aligned} \tag{45}$$

using the boundary conditions

$$\boldsymbol{G}(t_f) = \boldsymbol{S}, \tag{46}$$

$$\boldsymbol{g}(t_f) = \boldsymbol{S}\boldsymbol{Z}(t_f). \tag{47}$$

At the impulse epochs, $\boldsymbol{G}(t)$ and $\boldsymbol{g}(t)$ experience discontinuities, which can be solved by

$$\boldsymbol{G}(t_k^-) = \boldsymbol{Q}_k + \boldsymbol{C}_k^T(\boldsymbol{G}^{-1}(t_k^+) + \boldsymbol{D}_k\boldsymbol{R}_k^{-1}\boldsymbol{D}_k^T)^{-1}\boldsymbol{C}_k, \tag{48}$$

$$\begin{aligned}\boldsymbol{g}(t_k^-) = \boldsymbol{C}_k^T(\boldsymbol{G}^{-1}(t_k^+) \\ +\boldsymbol{D}_k\boldsymbol{R}_k^{-1}\boldsymbol{D}_k^T)^{-1}\boldsymbol{G}^{-1}(t_k^+)\boldsymbol{g}(t_k^+) + \boldsymbol{Q}_k\boldsymbol{Z}(t_k).\end{aligned} \tag{49}$$

Starting from the terminal condition $\boldsymbol{G}(t_f) = \boldsymbol{S}$ and $\boldsymbol{g}(t_f) = \boldsymbol{S}\boldsymbol{Z}(t_f)$, $\boldsymbol{G}(t)$ and $\boldsymbol{g}(t)$ are integrated backward using Eqs. (44) and (45) from t_f to t_{M-1}^+. At $t = t_{M-1}^+$, integration stops, and $\boldsymbol{G}(t_{M-1}^-)$ and $\boldsymbol{g}(t_{M-1}^-)$ are calculated using the discrete dynamics in Eqs. (48) and (49). Then, $\boldsymbol{G}(t_{M-1}^-)$ and $\boldsymbol{g}(t_{M-1}^-)$ are used as the new initial condition for integration in the time period from t_{M-1}^- to t_{M-2}^+, and so on and so forth.

3.4 Real-time control

The real-time control is a combination of the feedforward control and the linear feedback control, i.e., $\boldsymbol{u}_{\text{realtime}} = \boldsymbol{u}_{\text{feedforward}} + \boldsymbol{u}_{\text{feedback}}$. The feedforward control $\boldsymbol{u}_{\text{feedforward}}$ is generated by the open-loop hybrid LGL PS method in Sect. 3.1, and the feedback control $\boldsymbol{u}_{\text{feedback}}$ is obtained from the hybrid linear feedback controller discussed in Sect. 3.3 and given by Eqs. (42) and (43).

4 GEO debris removal

The control objective of removing GEO debris to the GEO graveyard region contains two aspects. On the one hand, the semi-major axis of the terminal orbit needs to be raised by 305 km. On the other hand, the eccentricity of the terminal orbit needs to be smaller than 10^{-4}. Consequently, the terminal perigee will be raised slightly more than 300 km, thereby it is within the GEO graveyard region.

In the simulation, the initial position of the satellite is set to be [0.0 m, 42164.8 km, 1.0 m] in the ECI frame, and the initial time is set as Jan 1st, 2017, 00:00:00, with the time constants $\Delta\text{UT}(\text{UT1} - \text{UTC}) = 0.359485$ s, $\Delta\text{AT}(\text{TAI} - \text{UTC}) = 37.0$ s. The removal time is chosen as 350 days; therefore, $t_f = 350$. The time step of the simulation 30 s. The A/m of the spacecraft is chosen as 0.13 m^2/kg.

4.1 Formulation and setup

We seek to minimize

$$\mathcal{J} = (\mid a_{t_f} - a_d \mid,\ \mid e_{t_f} - e_d \mid,\ V_t) \cdot \boldsymbol{S}_{ol}, \tag{50}$$

subject to

$$\begin{aligned} \dot{\boldsymbol{x}}(t) &= \boldsymbol{f}_c(\boldsymbol{x}(t), \boldsymbol{u}(t), t), \quad t \neq t_k, \\ \boldsymbol{x}(t_k^+) &= \boldsymbol{f}_d(\boldsymbol{x}(t_k^-), \boldsymbol{v}(t_k)), \quad t = t_k, \\ \boldsymbol{x}_l &\leq \boldsymbol{x}(t) \leq \boldsymbol{x}_u, \\ \boldsymbol{u}_l &\leq \boldsymbol{u}(t) \leq \boldsymbol{u}_u, \\ \boldsymbol{v}_l(t_k) &\leq \boldsymbol{v}(t_k) \leq \boldsymbol{v}_u(t_k), \\ \boldsymbol{x}(t_0) &= \boldsymbol{x}_0. \end{aligned} \tag{51}$$

Here, $a_d = 42164\,\text{km} + 305\,\text{km} = 42469\,\text{km}$ and $e_d = 10^{-4}$ are the desired semi-major axis and eccentricity, respectively. The quantity V_t is the magnitude of the total impulsive thrusts. The cost in Eq. (50) is a combination of the terminal cost (i.e., the terminal state error) and the discrete cost (i.e., the total magnitude of the impulses). The continuous and discrete dynamic equations are given by Eqs. (11) and (14), respectively, and t_k ($k = 1, ..., M-1$) represents the $M-1$ prescribed impulse time epochs. The lower bound of the state $\boldsymbol{x}_l = [42164 - 10\,\text{km},\ 0,\ 0,\ 0,\ 0,\ 0]^{\text{T}}$, and the upper bound $\boldsymbol{x}_u = [42164 + 350\,\text{km},\ 0.1,\ \frac{\pi}{180},\ 3\pi,\ 2\pi,\ 700\pi]^{\text{T}}$. The lower bound of the control angles $\boldsymbol{u}_l = [0,\ 0]^{\text{T}}$, and the upper bound $\boldsymbol{u}_u = [\frac{\pi}{2},\ 2\pi]^{\text{T}}$. The initial state $\boldsymbol{x}_0$ is given by the initial position of the satellite in the ECI frame. The results in reference [7] show that, when the removal time is 350 days and the A/m of spacecraft is equal to 0.13 m^2/kg, the terminal semi-major axis and eccentricity are close to the desired values; thus, only small impulses are required. After some trial and error, the upper bound magnitude of the impulsive thrusts in each direction is set to be 0.2 m/s. Thus, $\boldsymbol{v}_l(t_k) = -[0.2,\ 0.2,\ 0.2]^{\text{T}}$ m/s, $\boldsymbol{v}_u(t_k) = [0.2,\ 0.2,\ 0.2]^{\text{T}}$ m/s.

The hybrid optimal control problem in Eqs. (51) and (50) is converted into an NLP problem using the hybrid LGL PS method proposed in Sect. 3.1. The initial guess is the nominal trajectory solved in reference [7] excluding the first 20 days. This is because the argument of perigee and RAAN in the first 20 days exhibit oscillations. The oscillations are caused by the nature of GEO, since when the orbital initial eccentricity and inclination are small, the argument of perigee and RAAN will oscillate around 0° (360°) due to orbital perturbations. The oscillations are not favorable for polynomial approximations and will obstruct the convergence of the hybrid LGL PS method. Thus, in this work, the hybrid LGL PS optimization is focused on the last 330 days, and the real-time state at the end of the 20th day serves as the initial state. This initial guesses for the states and control are shown in Fig. 4. The corresponding terminal state error is +3.68 km for the semi-major axis and $+3.54 \cdot 10^{-4}$ for the eccentricity, respectively. The resulting terminal perigee is 10.58 km below the GEO graveyard threshold (42164.5 + 300 = 42464.5 km), thus impulsive thrusts are applied to assist the GEO debris removal. The initial guess for the cone angle α is chosen to be 0° (90°) when the satellite moves away from (toward) the Sun. Each of the 0° and 90° periods lasts about half an orbit (about 12 h for a GEO satellite). To capture this feature in the hybrid LGL PS method, the segment boundaries are chosen as the switching points of the cone angle; thus, the cone angle in each segment is either $\alpha = 0°$ or $\alpha = 90°$. The impulsive thrusts are designed to be applied at the segment boundaries, and the initial guesses for the impulsive thrusts are zero.

4.1.1 Implementation using receding horizon control

The hybrid LGL PS optimization is implemented through the receding horizon control described in [24], where the real-time state of the previous horizon serves as the initial state of the consecutive horizon. The horizon chosen in this work is one sidereal day. The optimization goal of each horizon day is to reduce the terminal semi-

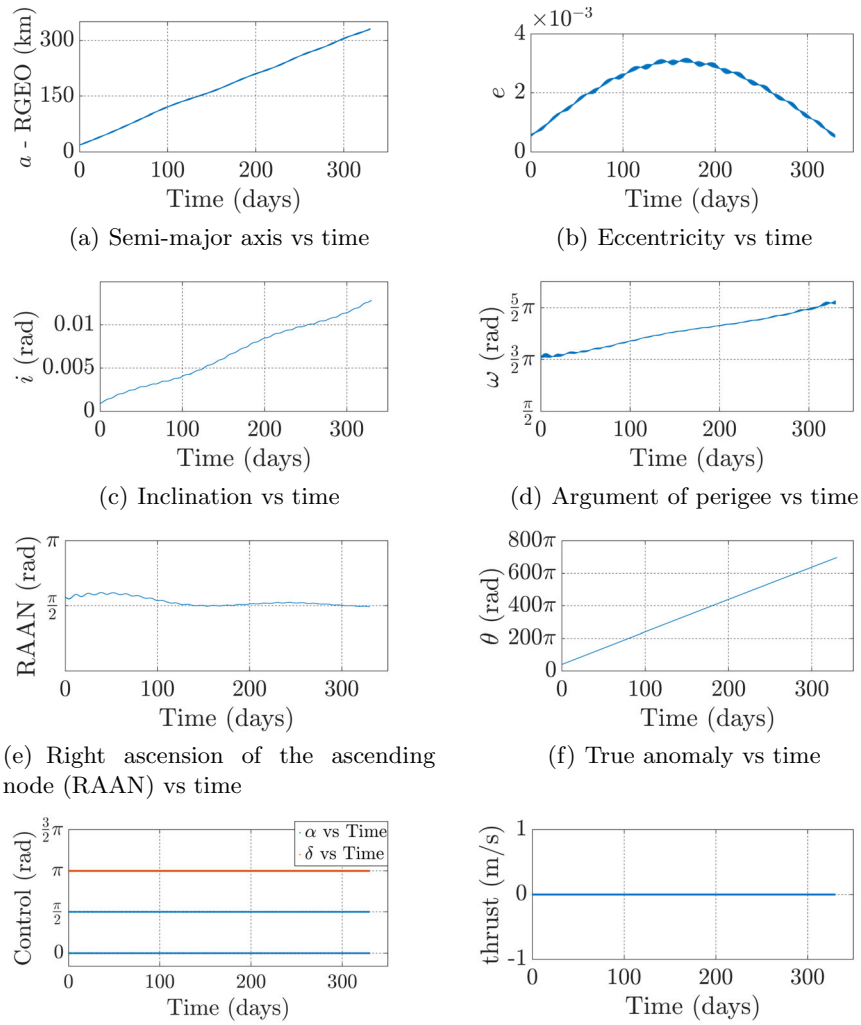

Fig. 4 The initial guesses for the states and control

major axis and eccentricity error in the initial guess by a portion of 1/330 (0.0112 km and $1.0751 \cdot 10^{-6}$ for semi-major axis and eccentricity, respectively. The removal time is 330 days). Specifically, at the end of the kth the horizon day, the desired semi-major axis $a_{dhor} = [(42, 164.8 + 305 + 3.6852) - k \cdot 0.0112]$ km, the desired eccentricity $e_{dhor} = 1 \cdot 10^{-4} + 3.5478 \cdot 10^{-4} - k \cdot 1.0751 \cdot 10^{-6}$, and $k = 1, 2, ..., 330$ is the number of horizon day.

4.2 Convergence test of the hybrid LGL PS method

In the convergence test, the simulation time is set to be the first 30 days of the GEO debris removal problem. For each segment in the hybrid PS method, 10, 15, 20, 25, 30 collocation points are applied in different sets of simulations. The penalty matrix in Eq. (50) is set to be $\boldsymbol{S}_{ol} = [1,\ 10^9,\ 1.5 \cdot 10^8]^{\mathrm{T}}$. The transcribed NLP problem is solved using SNOPT [28]. The Major Optimality and Feasibility Tolerance in SNOPT are both set to be 10^{-5}.

The unit of the impulse is m/s; thus, we can use ΔV to quantify the amount of the impulses. Table 1 and Fig. 5 present the state tracking error (relative to the desired state on each horizon day a_{dhor} and e_{dhor}) and the total ΔV of the impulses corresponding to the number of nodes applied per segment. We can see that as the number of nodes increases, the state tracking error and the total ΔV of the impulses decrease and at last converge to a small value. The positive error means that the terminal state is larger than the desired state.

4.3 Optimization using the hybrid LGL PS method

In the GEO debris removal problem, the simulation time is 330 days. The number of collocation points chosen is 30 for each segment. The penalty matrix in Eq. (50) is set to

Table 1 State tracking error and total ΔV of the impulses corresponding to different number of nodes applied per segment

Number of nodes	a Error (km)	e Error (10^{-7})	Total ΔV (m/s)
10	1.95	−164.50	14.04
15	−1.32	+1.72	7.90
20	0.20	+0.14	0.18
25	0.31	+27.06	0.12
30	−0.01	+0.13	0.10

Fig. 5 State tracking error and total ΔV of the impulses corresponding to different number of nodes applied per segment

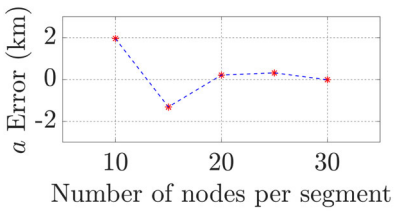

(a) Semi-major axis tracking error, relative to the desired value a_{dhor} on each horizon day

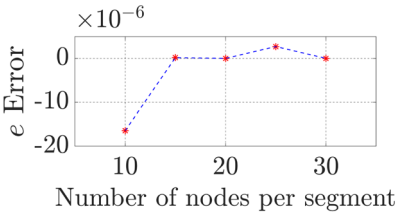

(b) Eccentricity tracking error, relative to the desired value e_{dhor} on each horizon day

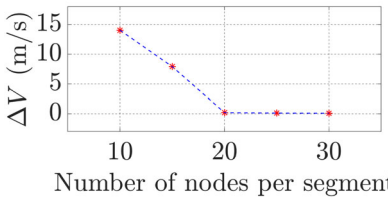

(c) Total ΔV of the impulses

be $\boldsymbol{S}_{ol} = [1,\ 10^9,\ 5 \cdot 10^9]^{\mathrm{T}}$. The NLP solver used is still SNOPT [28]. Because the goal of the open-loop hybrid PS optimization is to create a nominal trajectory for linearization, the optimization result does not to be accurate. Thus, the Major Optimality and Feasibility Tolerance for SNOPT are both set as 10^{-5} (which are larger than the default values 10^{-6}). In this way, the computation cost of the hybrid PS method is reduced.

The optimization results are presented in Fig. 6. After the hybrid LGL PS optimization, the terminal state error of the semi-major axis is reduced from +3.68 km to +3.53 km, while the eccentricity is reduced from $+3.54 \cdot 10^{-4}$ to $+6.30 \cdot 10^{-5}$. An amount of 2.78 m/s impulsive thrusts are consumed. The largest impulsive thrust reaches about 0.17 m/s, and occurs on the 128th horizon day (results shown in Fig. 7). From Fig. 7, we can see that the impulsive thrust is applied at the first segment boundary epoch, and it causes a jump in the semi-major axis error from 133.7 km to 134.0 km, and in the eccentricity error from $2.21 \cdot 10^{-3}$ to $2.22 \cdot 10^{-3}$. The real-time control, semi-major axis, and eccentricity error are presented in Fig. 8. The maximal changing rate of the control angles is about 16 degrees per minute.

It can be seen from Fig. 6 that the solution generated by the open-loop hybrid LGL PS method is locally optimal. Because the terminal semi-major axis is 3.53 km larger than the desired one, and the spare orbit height can be used to further reduce the orbit eccentricity and the magnitude of the total impulsive thrusts, thus reducing the cost function. In the next section, the hybrid linear feedback controller developed in Sect. 3.3 will be applied to further reduce the terminal state error and the cost function, thus stabilizing the open-loop hybrid LGL PS method.

4.4 Optimization using the hybrid feedback pseudospectral method

In this section, the dynamic system is first linearized along the locally optimal trajectory generated by the open-loop hybrid LGL PS method, and then, the hybrid linear feedback controller designed in Sect. 3.3 is used to stabilize the open-loop hybrid LGL PS method. The real-time control applied is a combination of the feedforward and feedback controls, i.e., $\boldsymbol{u}_{\text{realtime}} = \boldsymbol{u}_{\text{feedforward}} + \boldsymbol{u}_{\text{feedback}}$, where $\boldsymbol{u}_{\text{feedforward}}$ is the solution of the open-loop hybrid LGL PS method, as shown in Fig. 6, and $\boldsymbol{u}_{\text{feedback}}$ is the linear feedback control presented in Eqs. (42) and (43). The control objective is to reduce the terminal semi-major axis and eccentricity error. Thus, in the penalty matrix $\boldsymbol{S}$ and $\boldsymbol{Q}$, we make the first two parameters relatively larger. We want to focus on the terminal state error; thus, we make the elements in $\boldsymbol{S}$ relatively

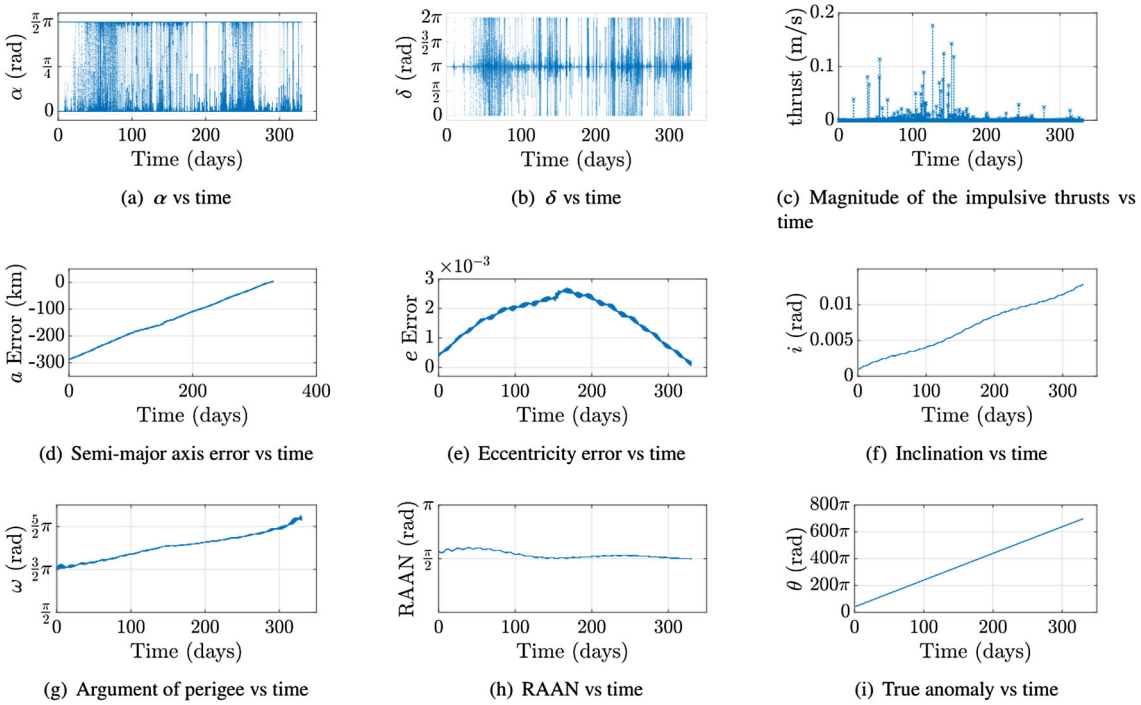

(a) α vs time (b) δ vs time (c) Magnitude of the impulsive thrusts vs time

(d) Semi-major axis error vs time (e) Eccentricity error vs time (f) Inclination vs time

(g) Argument of perigee vs time (h) RAAN vs time (i) True anomaly vs time

Fig. 6 Real-time control and states, optimization using the hybrid LGL PS method

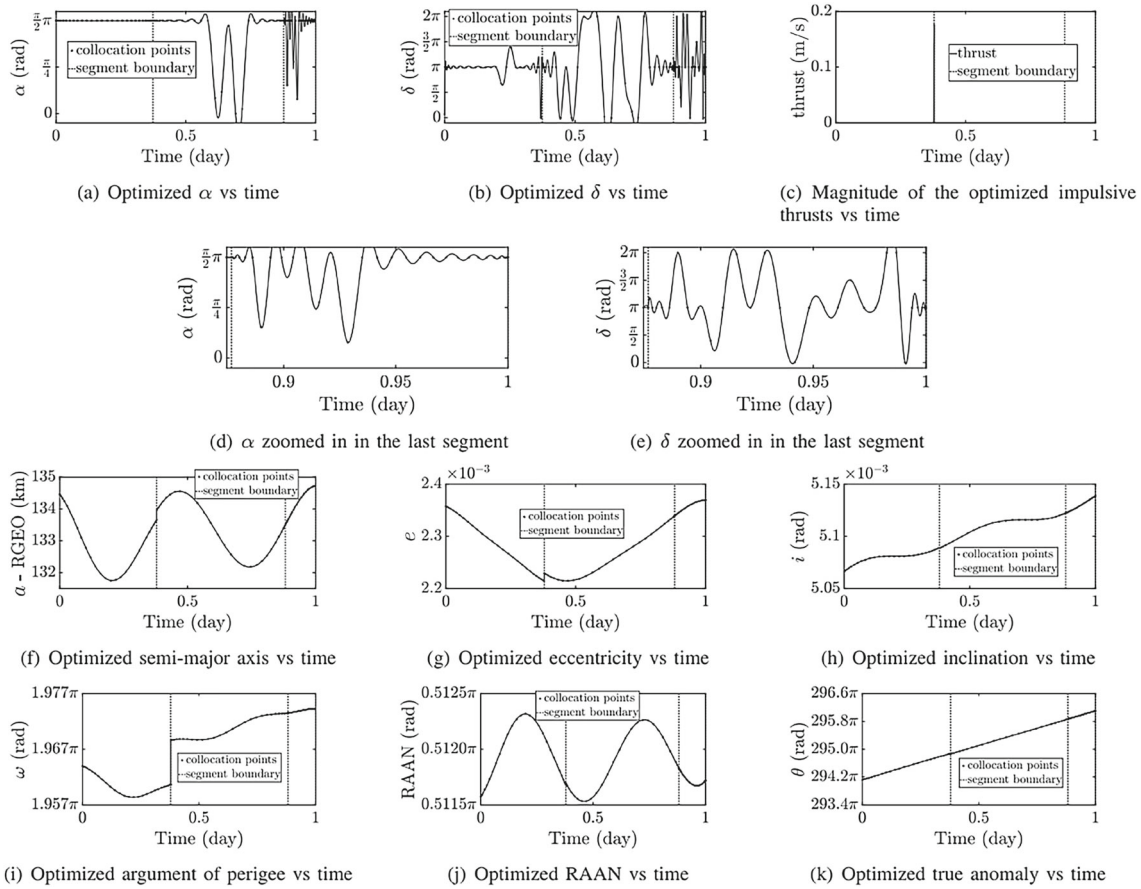

(a) Optimized α vs time (b) Optimized δ vs time (c) Magnitude of the optimized impulsive thrusts vs time

(d) α zoomed in in the last segment (e) δ zoomed in in the last segment

(f) Optimized semi-major axis vs time (g) Optimized eccentricity vs time (h) Optimized inclination vs time

(i) Optimized argument of perigee vs time (j) Optimized RAAN vs time (k) Optimized true anomaly vs time

Fig. 7 Optimized control and states, optimization using the hybrid LGL PS method on the 128th horizon day

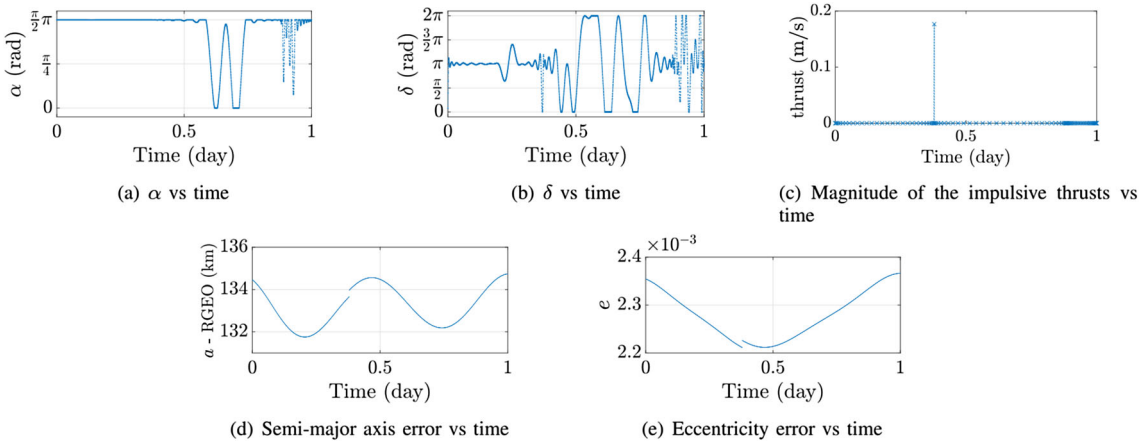

(a) α vs time (b) δ vs time (c) Magnitude of the impulsive thrusts vs time

(d) Semi-major axis error vs time (e) Eccentricity error vs time

Fig. 8 Real-time control and states, optimization using the hybrid LGL PS method on the 128th horizon day

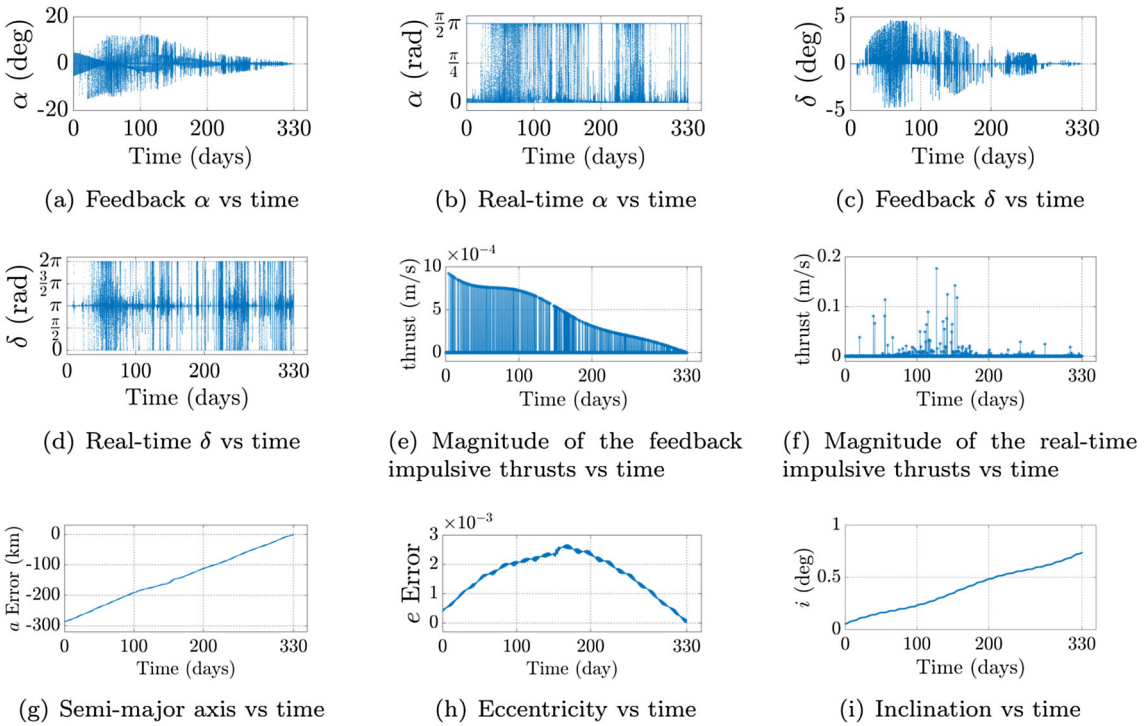

(a) Feedback α vs time (b) Real-time α vs time (c) Feedback δ vs time

(d) Real-time δ vs time (e) Magnitude of the feedback impulsive thrusts vs time (f) Magnitude of the real-time impulsive thrusts vs time

(g) Semi-major axis vs time (h) Eccentricity vs time (i) Inclination vs time

Fig. 9 Real-time control and states, optimization using the hybrid feedback PS method

larger than the elements in $\boldsymbol{Q}$. We want to use as little fuel as possible; thus, the penalty matrix $\boldsymbol{R}_k$ is chosen as large as possible. Through appropriate tuning, the penalty matrices in Eq. (41) are chosen as $\boldsymbol{S} = \text{diag}[10^3,\ 10^{20},\ 1,\ 1,\ 1,\ 1]$, $\boldsymbol{Q} = \text{diag}[1,\ 10^8,\ 1,\ 1,\ 1,\ 1]$, $\boldsymbol{R} = 1.5 \cdot 10^{15} \cdot \boldsymbol{I}_2$, $\boldsymbol{Q}_k = \boldsymbol{I}_6$, $\boldsymbol{R}_k = 3.5 \cdot 10^{23} \cdot \boldsymbol{I}_3$, where $\boldsymbol{I}_n$ $(n = 2, 3, 6)$ is the $n \times n$ identity matrix.

The optimization results are shown in Fig. 9. The feedback α and δ are around 10° and 3°, respectively, and are gradually converging to 0°. The magnitude of the total feedback impulsive thrusts is 0.15 m/s, which results in a reduction of 0.06 m/s in the magnitude of the total real-time impulsive thrusts. Note that 0.15 m/s > 0.06 m/s is the result of vector addition of the nominal and feedback impulsive thrusts. After the hybrid feedback PS optimization, the terminal state error of the semi-major axis is reduced from +3.53 km to +0.08 km, and the eccentricity is reduced from $+6.30 \cdot 10^{-5}$ to $-8.04 \cdot 10^{-7}$. Consequently, the cost value is reduced from $1.39 \cdot 10^{10}$ to $1.36 \cdot 10^{10}$. The terminal state error and the cost value are further reduced by the hybrid linear feedback controller, and the optimization accuracy is improved. As a result a conclusion can be drawn that the open-loop hybrid

Table 2 History of the terminal state error and the total ΔV of the required impulsive thrusts

Optimization step	Terminal a error (km)	Terminal e error	Total ΔV (m/s)
Initial guess	+3.68	$+3.54 \cdot 10^{-4}$	–
Hybrid PS method	+3.53	$+6.30 \cdot 10^{-5}$	2.78
Hybrid feedback PS method	+0.08	$-8.04 \cdot 10^{-7}$	2.73

LGL PS method is stabilized by the hybrid linear feedback controller.

5 Conclusion and future work

This paper first extends the local LGL PS method to a hybrid LGL PS method which is capable of solving hybrid nonlinear optimal control problems. Then, a hybrid feedback PS method is proposed, in which a hybrid linear feedback controller is developed to stabilize the open-loop hybrid LGL PS method when it converges to a local minimum. Simulations indicate that GEO debris are successfully removed to the GEO graveyard region using SRP and impulsive thrusts in conjunction with the proposed hybrid feedback PS method. The terminal state error of semi-major axis and eccentricity in reference [7] are reduced from +28.64 km to +0.08 km, and from $+7.26 \cdot 10^{-4}$ to $-8.04 \cdot 10^{-7}$, respectively, and the total ΔV of the required impulsive thrusts is significantly reduced from 10.59 m/s to 2.73 m/s.

Rigorous proofs of the stability and convergence properties of the hybrid feedback PS method are not contained in this work. It is challenging to prove the stability and the convergence properties of a time-varying optimal control method whose time span is $[0,\ t_f]$ (t_f is some prescribed terminal time). For an LTI system, we can prove the convergence properties and the stability in the Lyapunov sense of an LQR controller on an infinite time interval, because the solution of the algebraic Riccati equation is a constant matrix. However, when the dynamic system is time-varying and on a finite time interval, the solution of the Riccati equation goes time-varying. In this case, the solution of the Riccati equation depends on the LTV system, and this makes it challenging to derive general stability and convergence property conclusions. In this work, we have used numerical examples to show the convergence of the hybrid LGL PS method and the validity of the proposed feedback PS method. We leave the stability and convergence proofs to future work.

Funding The authors have not disclosed any funding.

Declarations

Conflict of interest The authors have not disclosed any competing interests.

References

1. Anderson PV, Schaub H (2014) Local debris congestion in the geosynchronous environment with population augmentation. Acta Astronaut 94(2):619–628
2. McKnight DS, Di Pentino FR (2013) New insights on the orbital debris collision hazard at geo. Acta Astronaut 85:73–82
3. Oltrogge D, Alfano S, Law C, Cacioni A, Kelso T (2018) A comprehensive assessment of collision likelihood in geosynchronous earth orbit. Acta Astronaut 147:316–345
4. S. Group and W. G. 4 (2007) Space debris mitigation guidelines. Inter-Agency Space Debris Coordination Committee. Toulouse, France. Revision 1. Sep. 2007. [Online]. Available: http://www.unoosa.org/documents/pdf/spacelaw/sd/IADC-2002-01-IADC-Space_Debris-Guidelines-Revision1.pdf
5. Borja JA, Tun D (2006) Deorbit process using solar radiation force. J Spacecr Rocket 43(3):685–687
6. Kelly PW, Bevilacqua R, Mazal L, Erwin RS (2018) Tugsat: removing space debris from geostationary orbits using solar sails. J Spacecr Rocket 55(2):437–450
7. Mei H, Damaren CJ, Zhan X (2020) Hybrid removal of end-of-life geosynchronous satellites using solar radiation pressure and impulsive thrusts. Adv Space Res 66(4):974–991
8. Mei H, Damaren CJ, Zhan X (2022) Feedback pseudospectral method for end-of-life geostationary satellites removal using solar sailing. J Guidance Control Dyn 45(3):570–579
9. Mei H, Damaren CJ, Zhan X (2021) End-of-life geostationary satellite removal using realistic flat solar sails. Aerospace Syst 4(3):227–238
10. Conway BA (2012) A survey of methods available for the numerical optimization of continuous dynamic systems. J Optim Theory Appl 152(2):271–306
11. Ross IM, Fahroo F (2004) Legendre pseudospectral approximations of optimal control problems. In: New trends in nonlinear dynamics and control and their applications. Springer, pp 327–342
12. Benson DA, Huntington GT, Thorvaldsen TP, Rao AV (2006) Direct trajectory optimization and costate estimation via an orthogonal collocation method. J Guid Control Dyn 29(6):1435–1440
13. Elnagar G, Kazemi MA, Razzaghi M (1995) The pseudospectral legendre method for discretizing optimal control problems. IEEE Trans Autom Control 40(10):1793–1796
14. Fahroo F, Ross IM (2001) Costate estimation by a legendre pseudospectral method. J Guid Control Dyn 24(2):270–277
15. Garg D, Patterson MA, Francolin C, Darby CL, Huntington GT, Hager WW, Rao AV (2011) Direct trajectory optimization and costate estimation of finite-horizon and infinite-horizon optimal control problems using a radau pseudospectral method. Comput Optim Appl 49(2):335–358
16. Huntington G, Benson D, Rao A (2007) A comparison of accuracy and computational efficiency of three pseudospectral methods. In: AIAA guidance, navigation and control conference and exhibit, pp 6405
17. Garg D, Patterson M, Hager WW, Rao AV, Benson DA, Huntington GT (2010) A unified framework for the numerical solution of optimal control problems using pseudospectral methods. Automatica 46(11):1843–1851

18. Williams P (2009) Hermite-legendre-gauss-lobatto direct transcription in trajectory optimization. J Guid Control Dyn 32(4):1392–1395
19. Rao AV (2009) A survey of numerical methods for optimal control. Adv Astronaut Sci 135(1):497–528
20. Huntington GT, Rao AV (2008) Comparison of global and local collocation methods for optimal control. J Guid Control Dyn 31(2):432–436
21. Narayanaswamy S, Damaren CJ (2020) Comparison of the legendre–gauss pseudospectral and hermite–legendre–gauss–lobatto methods for low-thrust spacecraft trajectory optimization. Aerospace Syst pp 1–18
22. Ross I, Sekhavat P, Fleming A, Gong Q, Kang W (2006) Pseudospectral feedback control: foundations, examples and experimental results. In: AIAA guidance, navigation, and control conference and exhibit, p 6354
23. Bollino KP, Ross IM (2007) A pseudospectral feedback method for real-time optimal guidance of reentry vehicles. In: 2007 American Control Conference. IEEE, pp 3861–3867
24. Yan H, Ross IM, Alfriend KT (2007) Pseudospectral feedback control for three-axis magnetic attitude stabilization in elliptic orbits. J Guid Control Dyn 30(4):1107–1115
25. McInnes CR (1999) Solar sailing: technology, dynamics and mission applications. Springer, Berlin
26. Vallado DA (2001) Fundamentals of astrodynamics and applications. Springer, New York
27. Hughes PC (2012) Spacecraft attitude dynamics. Courier Corporation
28. Gill PE, Murray W, Saunders MA (2005) Snopt: an sqp algorithm for large-scale constrained optimization. SIAM Rev 47(1):99–131